



Resilient GNSS real-time kinematic precise positioning with inequality and equality constraints

Zhetao Zhang¹ · Yuan Li¹ · Xiufeng He¹ · Lita Hsu²

Received: 27 December 2022 / Accepted: 7 April 2023 / Published online: 26 April 2023
© The Author(s), under exclusive licence to Springer-Verlag GmbH Germany, part of Springer Nature 2023

Abstract

How to conduct the GNSS real-time kinematic precise positioning in challenging environments is not an easy problem. The challenging environment mainly refers to frequent signal reflection, refraction, diffraction, and occlusion, inevitably introducing large positioning errors. We propose a resilient positioning method considering the inequality and equality constraints. Specifically, first, we introduce the functional and stochastic models of real-time kinematic (RTK) positioning, considering the impacts of challenging environments. Second, specific iterative procedures of resilient GNSS precise positioning method with inequality and equality constraints are proposed. In addition, a general form of inequality constraints in terms of coordinate components is given that is suitable for real-time kinematic situations. Four 24-h real datasets in canyon environments were collected to verify the performance of the proposed method. The results show that compared with the traditional RTK positioning without inequality constraints, the proposed method can improve the success rates of ambiguity resolution by 42.2% on average. Also, the positioning accuracy of fixed solutions can be improved significantly after applying the proposed method, where the root mean square errors can be reduced by 77.2% on average. Therefore, the proposed method can significantly improve success rates of ambiguity resolution and positioning accuracy, which is especially promising in challenging environments.

Keywords GNSS · Real-time kinematic situation · Resilient positioning · Inequality constraint · Challenging environment

Introduction

GNSS real-time kinematic precise positioning has been widely used in many areas, such as high-precision monitoring and intelligent transportation. In the most commonly used approach, real-time kinematic (RTK) positioning, since the observation condition at this time is usually in a challenging environment such as urban or rural canyons, the signals are easily reflected, refracted, diffracted, and even blocked, which will usually cause site-specific observation errors. This type of phenomenon will hinder positioning performance (Sun et al. 2021). Hence, accurately conducting

the GNSS real-time and kinematic positioning, especially under challenging circumstances, is a tricky problem.

Many efforts have been made how to obtain high-precision and high-reliability positioning. First of all, mathematical refinement is widely investigated, where the functional model compensation (Zhong et al. 2010; Marques et al. 2011) and the stochastic model compensation (Schön and Brunner 2008; Luo et al. 2014) are both discussed. The main reason is that residual observation errors always exist at this time. Here, the residual observation error mainly refers to the generalized unmodeled error which cannot be eliminated or easily mitigated by differencing and combination of observations, model correction, and parameterization, mainly including the colored noise, residual systematic errors, and other special outliers (Li et al. 2018; Zhang et al. 2019). Specifically, ignoring the satellite end, they can be mainly divided into two categories: site-specific unmodeled error and path-dependent unmodeled error. The first one mainly includes the multipath effects, diffraction, and non-line-of-sight (NLOS) reception (Zhang et al. 2022c), and the second one primarily refers to the residual atmospheric delays such

✉ Xiufeng He
xfhe@hhu.edu.cn

¹ School of Earth Sciences and Engineering, Hohai University, Nanjing 211100, China

² Department of Aeronautical and Aviation Engineering, The Hong Kong Polytechnic University, Hung Hom, Hong Kong, China

as higher-order ionospheric effects and wet tropospheric effects (Zhang and Li 2020).

Since there is usually externally available information, external information assistance has been explored. Specifically, multi-sensor fusion is effective, including using IMU (Petovello and Lachapelle 2006), LiDAR (Chang et al. 2019), vision (Meguro et al. 2009), etc. Also, high-precision maps or accurate building models can be considered. Based on this, several specific strategies such as ray tracing (Lau and Cross 2007), shadow matching (Wang et al. 2015), and 3D mapping aiding (Ng and Hsu 2021) are proposed. However, this approach is usually a little complicated, with low efficiency and high cost. On the other hand, internal conditions have also been applied to the GNSS community. For instance, the motion state of the carrier, such as velocity and trajectory, can be considered (Zhou and Li 2016). The baseline length constraint can also be used in ambiguity resolution and positioning (Teunissen et al. 2011; Ma et al. 2021). Moreover, in a real-time kinematic situation, the non-holonomic constraint (Saurabh 2006; Zhang et al. 2022b) is another feasible strategy, especially in urban canyon environments. The most significant limitation of this approach is that the constraints need to be accurate and reliable enough; otherwise, these constraints would be counterproductive.

Actually, the above methods are all essentially equality constraints. If these constraints exist but are not trustworthy enough, the corresponding degraded inequality constraints are apparently more reliable. As a trial, Lu et al. (1993) introduced the application of inequality constraint in GPS navigation in the case of selective availability. Although this approach has been devoted to the areas of geodesy by several researchers (Zhu et al. 2005; Xie et al. 2022), little attention has been paid to the application of inequality constraints in the current GNSS community, especially under challenging circumstances. Actually, the inequality constraints are widely existent in real applications such as the constraints of the coordinates. To implement high-precision and high-reliability positioning, navigation, and timing (PNT), the inequality-constrained method is essentially an important idea of resilient PNT (Yang 2018), where the mathematical model may be adjusted according to reality.

We first propose a resilient real-time kinematic precise positioning method with inequality and equality constraints in a programmatically easy way, which is especially suitable for challenging environments. First, the functional and stochastic models of RTK positioning in challenging environments are given and discussed. Second, specific iterative procedures of resilient GNSS precise positioning method with inequality and equality constraints are proposed, and a general form of inequality constraints considering the coordinate difference between adjacent epochs is given that is suitable for the real-time kinematic situation. Finally, four real datasets in canyon

environments were collected to verify the performance of the proposed method, and some conclusions are made.

Basic model of GNSS real-time kinematic precise positioning

As the most important means of real-time kinematic precise positioning, i.e., RTK, the mathematical model is discussed briefly, including the functional and stochastic models. Also, the characteristics of these two models in challenging environments are analyzed theoretically.

The functional model aims to establish the relationship between the observations and the unknown parameters. In RTK positioning of challenging environments, the general double-difference (DD) code and phase measurements on frequency i of a single constellation read (Leick et al. 2015)

$$\nabla \Delta P_{qr,i}^{kl} = \nabla \Delta \rho_{qr}^{kl} + \nabla \Delta I_{qr,i}^{kl} + \nabla \Delta T_{qr}^{kl} + \nabla \Delta M_{qr,i}^{kl} + \nabla \Delta U_{qr,i}^{kl} \tag{1}$$

$$\nabla \Delta \Phi_{qr,i}^{kl} = \nabla \Delta \rho_{qr}^{kl} + \lambda_i \nabla \Delta N_{qr,i}^{kl} - \nabla \Delta I_{qr,i}^{kl} + \nabla \Delta T_{qr}^{kl} + \nabla \Delta m_{qr,i}^{kl} + \nabla \Delta \mu_{qr,i}^{kl} \tag{2}$$

where operators “ ∇ ” and “ Δ ” express the between-satellite and between-receiver differences, superscripts “ k ” and “ l ” the reference and common satellites, subscripts “ q ” and “ r ” the base and rover receivers, P and Φ the code and phase observations, ρ and λ the receiver-satellite range and wavelength, I and T the ionospheric and tropospheric delays, M and m the code and phase multipath errors, U and μ the code and phase observation noise, and N is the integer ambiguity.

In RTK positioning of challenging environments, the atmospheric delays can be mitigated or even eliminated in the case of a short baseline, and then, the general linear functional model of DD measurements can be deduced as

$$\begin{bmatrix} P \\ \phi \end{bmatrix} = \begin{bmatrix} e_f \otimes a_l & 0 \\ e_f \otimes a_l & b_f \otimes I_l \end{bmatrix} \begin{bmatrix} x \\ N \end{bmatrix} + \begin{bmatrix} \tilde{U} \\ \tilde{\mu} \end{bmatrix} \tag{3}$$

with $P = [P_1^T, \dots, P_f^T]^T$, $P_f = [\nabla \Delta P_{qr,f}^{k1}, \dots, \nabla \Delta P_{qr,f}^{kl}]^T$, $\phi = [\phi_1^T, \dots, \phi_f^T]^T$, $\phi_f = [\nabla \Delta \phi_{qr,f}^{k1}, \dots, \nabla \Delta \phi_{qr,f}^{kl}]^T$, $x = [dx, dy, dz]^T$, $N = [N_1^T, \dots, N_f^T]^T$, $N_f = [\nabla \Delta N_{qr,f}^{k1}, \dots, \nabla \Delta N_{qr,f}^{kl}]^T$, $\tilde{U} = [\tilde{U}_1^T, \dots, \tilde{U}_f^T]^T$, $\tilde{U}_f = [\nabla \Delta \tilde{U}_{qr,f}^{k1}, \dots, \nabla \Delta \tilde{U}_{qr,f}^{kl}]^T$, $\tilde{\mu} = [\tilde{\mu}_1^T, \dots, \tilde{\mu}_f^T]^T$, $\tilde{\mu}_f = [\nabla \Delta \tilde{\mu}_{qr,f}^{k1}, \dots, \nabla \Delta \tilde{\mu}_{qr,f}^{kl}]^T$, where P and ϕ express the code and phase observation vector, x and N the unknown coordinate components and integer ambiguities, \tilde{U} and $\tilde{\mu}$ the code and phase observation noise and unmodeled errors, e_f and I_l the $f \times 1$ matrix with all elements of 1 and

the $l \times l$ identity matrix, a_l the $l \times 3$ design matrix of x , $b_f = \text{diag}(\lambda_1, \dots, \lambda_f)$ the $f \times f$ design matrix of N , and operators “ \otimes ” and “diag” are the Kronecker product and diagonal concatenation of elements, respectively.

Based on (3), the multi-GNSS functional model can be simplified as

$$L = AX + E \tag{4}$$

where L expresses the observation vector, A the design matrix of the unknown parameters, X the coordinate components and ambiguities, and E the observation noise and residual observation error vector.

The stochastic model reflects the precisions and correlations of the observations using a variance–covariance matrix, which can be estimated based on the residuals of measurements. According to the law of covariance propagation, the DD variance–covariance matrix can be expressed as

$$D = (I_{2f} \otimes O)F(I_{2f} \otimes O)^T \tag{5}$$

where $O = [-e_l, I_l, e_l, -I_l]$ expresses the transformation matrix of the undifferenced to DD variance–covariance matrix and F is the variance–covariance matrix of undifferenced observations.

By performing least squares adjustment, the estimated unknown parameters \hat{X} and corresponding variance–covariance matrix $D_{\hat{X}}$ can be derived as

$$\hat{X} = (A^T D^{-1} A)^{-1} A^T D^{-1} L \tag{6}$$

$$D_{\hat{X}} = (A^T D^{-1} A)^{-1} \tag{7}$$

where D expresses the variance–covariance matrix of DD observations. The float solution can be obtained by (6) and (7), and then, the real values of ambiguities need to be fixed to integer values. After verifying the validity of integer ambiguity, the baseline can be updated to obtain the final estimated coordinate parameters.

Resilient RTK positioning with inequality and equality constraints

A resilient RTK positioning model with equality and inequality constraints is proposed in this section, and then, a general form of inequality constraints in terms of coordinate components is given and discussed in detail.

Methodology of resilient RTK positioning with inequality and equality constraints

In real applications, internal or external constraints are always available. If they can be precisely determined, the equality constraints, e.g., the state equation, can be adopted. Otherwise, if these constraints exist but are not very precise or very strong, the inequality constraints can be used in theory. As mentioned above, this is like the idea of resilient PNT. Hereafter, the proposed method can be called the resilient RTK positioning. If equality and inequality constraints are available, the resilient RTK positioning model can be expressed as

$$\begin{cases} L_k = A_k X_k + E_k \\ X_k = \Psi_{k, k-1} \hat{X}_{k-1} + W_k \\ \Gamma_k X_k \leq G_k \end{cases} \tag{8}$$

where k expresses the epoch number, $\Psi_{k, k-1}$ the state transition matrix of adjacent epochs, \hat{X}_{k-1} the estimated parameters in the $(k - 1)$ th epoch, W_k the state noise, Γ_k the design matrix of inequality constraints, and G_k the constant vector of inequality constraints. The first sub-equation is an observation equation, and the second sub-equation is a state equation (i.e., equality constraint). Then, the third sub-inequation is an inequality constraint. The specific steps of resilient RTK positioning with equality and inequality constraints are given below, which is essentially an iterative procedure.

First, for the estimation of the iterative initial value, only the first and second sub-equations are used for the solution, that is, the Kalman filter model, which can enhance the precision and reliability of RTK positioning and has the following form

$$\begin{cases} L_k = A_k X_k + E_k \\ X_k = \Psi_{k, k-1} \hat{X}_{k-1} + W_k \end{cases} \tag{9}$$

Using the widely used extended Kalman filter (EKF) method as an example, the initial iterative solution of the EKF can be obtained as

$$\hat{X}_k^{(0)} = \bar{X}_k + K_k (L_k - A_k \bar{X}_k) \tag{10}$$

where $\bar{X}_k = \Psi_{k, k-1} \hat{X}_{k-1}$ expresses the predicted parameters and $K_k = D_{\bar{X}_k} A_k^T (A_k D_{\bar{X}_k} A_k^T + D_k)^{-1}$ is the gain matrix. Correspondingly, the variance–covariance matrix of the estimated parameters reads

$$D_{\hat{X}_k^{(0)}} = (I_k - K_k A_k) D_{\bar{X}_k} \tag{11}$$

where $D_{\bar{X}_k} = \Psi_{k, k-1} D_{\hat{X}_{k-1}} \Psi_{k, k-1}^T + D_{W_k}$ expresses the variance–covariance matrix of the predicted parameters, D_k the

variance–covariance matrix of observations in the k th epoch, $D_{\hat{X}_{k-1}}$ the variance–covariance matrix of the estimated parameters in the $(k - 1)$ th epoch, and D_{W_k} is the variance–covariance matrix of the state noise.

Second, check whether $\hat{X}_k^{(0)}$ satisfies the third sub-inequation of (8), and then,

$$\Gamma_k \hat{X}_k^{(0)} \leq G_k \tag{12}$$

The core question of inequality constraints is how to appropriately use (12) in reality; hence, let us have a category discussion. If the inequation is satisfied for every inequality constraint, i.e., $\Gamma_k \hat{X}_k^{(0)} - G_k \leq 0$, we can ignore this constraint directly. If the inequation is not satisfied, i.e., $\Gamma_k \hat{X}_k^{(0)} - G_k > 0$, the inequality constraints need to be considered. Hence, it follows that the judgment vector of inequality validity $J^{(0)}$, defined as

$$J^{(0)} = \Gamma_k \hat{X}_k^{(0)} - G_k \tag{13}$$

Specifically, if $J_m^{(0)} > 0$ with m denoting the index of constraints, it can be called a valid constraint; otherwise, it is an invalid constraint that can be ignored. Therefore, we can output $\hat{X}_k = \hat{X}_k^{(0)}$, directly provided that $J^{(0)} \leq 0$. Otherwise, for ease of calculation, a so-called penalty function $P^{(0)}$ is introduced to turn inequality constraints into equality constraints (Zhu and Xie 2011). The variance element of the weight matrix of the penalty function P^0 can be deduced as

$$P_m^{(0)} = \begin{cases} \zeta J_m^{(0)} > 0 \\ \xi J_m^{(0)} \leq 0 \end{cases} \tag{14}$$

where ζ is a very large value (e.g., 100,000), while ξ is a very small value (e.g., 0.00001). Of course, these two values can be changed according to the accuracy and reliability of the inequality constraints. Then, the variance–covariance matrix of the penalty function can be described as

$$D_J^{(0)} = P^{(0)-1} \tag{15}$$

Based on this, a virtual observation equation can be built

$$G_k = \Gamma_k X_k + H_k \tag{16}$$

where H_k expresses the virtual observation error vector, of which the variance–covariance matrix is $D_J^{(0)}$ at this time.

Third, according to the generalized least squares criterion, the virtual observation equation (16) can be added to the first sub-equation of (9). The augmented observation equation can be described as

$$L'_k = A'_k X_k + E'_k \tag{17}$$

where $L'_k = [L_k^T, G_k^T]^T$ expresses the augmented observation vector, $A'_k = [A_k; \Gamma_k]$ the augmented design matrix, and

$E'_k = [E_k^T, H_k^T]^T$ is the augmented observation error vector. Using the form of Kalman filter recursive solution, the first iterative solution $\hat{X}_k^{(1)}$ and its covariance matrix $D_{\hat{X}_k^{(1)}}$ are obtained as

$$\hat{X}_k^{(1)} = \hat{X}_k^{(0)} + K_k^{(0)} (L'_k - A'_k \hat{X}_k^{(0)}) \tag{18}$$

$$D_{\hat{X}_k^{(1)}} = (I_k - K_k^{(0)} A'_k) D_{\hat{X}_k^{(0)}} \tag{19}$$

where $K_k^{(0)} = D_{\hat{X}_k^{(0)}} A_k'^T (A_k' D_{\hat{X}_k^{(0)}} A_k'^T + D_k^{(0)})^{-1}$ expresses the augmented gain matrix, $D_k^{(0)} = \text{blkdiag}(D_k, D_J^{(0)})$ the augmented variance–covariance matrix of observations, and operator “blkdiag” is the block diagonal concatenation of matrices.

Finally, since there is no guarantee that the estimated parameters can all satisfy inequation (12) after one iteration, if necessary, repeat the second and third steps until $\hat{X}_k^{(s)}$ totally satisfies inequation (12). Therefore, the final estimated parameters read

$$\hat{X}_k = \begin{cases} \bar{X}_k + K_k (L_k - A_k \bar{X}_k) & s = 0 \\ \hat{X}_k^{(s-1)} + K_k^{(s-1)} (L'_k - A'_k \hat{X}_k^{(s-1)}) & s \geq 1 \end{cases} \tag{20}$$

The corresponding variance–covariance matrix reads

$$D_{\hat{X}_k} = \begin{cases} (I_k - K_k A_k) D_{\bar{X}_k} & s = 0 \\ (I_k - K_k^{(s-1)} A'_k) D_{\hat{X}_k^{(s-1)}} & s \geq 1 \end{cases} \tag{21}$$

where s ($s \geq 0$) expresses the number of iterations, and $K_k^{(s-1)} = D_{\hat{X}_k^{(s-1)}} A_k'^T (A_k' D_{\hat{X}_k^{(s-1)}} A_k'^T + D_k^{(s-1)})^{-1}$ is the augmented gain matrix. Since the estimated parameters contain ambiguities according to (4), the float solution can be obtained by (20) and (21), and then, the fixed solution can be deduced after the ambiguity resolution and validation.

A general form of inequality constraints in real-time kinematic precise positioning

As usual, the users are more concerned with the positioning results of three directions. As an exploration, a general form of inequality constraints is given in this study for the challenging environment. That is, the precise coordinates $x_k = [x_k, y_k, z_k]^T$ are discussed. Certainly, the other parameters, such as ambiguities, can also be considered if necessary. First, in real-time and kinematic situations, the precisely known coordinates cannot always be easily determined in advance. Hence, the dynamic constraints are more

appropriate. In this study, the coordinate difference between adjacent epochs, i.e., between the $(k - 1)$ th and k th epochs ($k > 1$), is considered.

Assuming $\mathbf{x}_{k-1} = [x_{k-1}, y_{k-1}, z_{k-1}]^T$ are determined precisely, two kinds of constraints are added here. One is a horizontal constraint in the directions of e (east direction E) and n (north direction N), which can be described as

$$\alpha_1 \leq e_k - e_{k-1} \leq \alpha_2 \tag{22}$$

$$\beta_1 \leq n_k - n_{k-1} \leq \beta_2 \tag{23}$$

where $\alpha_1, \alpha_2, \beta_1,$ and β_2 express the horizontal constraint parameters. The other one is a vertical constraint in u (up direction U), which can be described as

$$\gamma_1 \leq u_k - u_{k-1} \leq \gamma_2 \tag{24}$$

where γ_1 and γ_2 express the vertical constraint parameters.

Since the coordinate system is an earth-centered earth-fixed coordinate system, one needs to convert the geodetic coordinates to the topocentric coordinates by using the following equation

$$\begin{bmatrix} e_k \\ n_k \\ u_k \end{bmatrix} = T \begin{bmatrix} x_k - x_0 \\ y_k - y_0 \\ z_k - z_0 \end{bmatrix} \tag{25}$$

where $T = \begin{bmatrix} -\sin(L_0) & \cos(L_0) & 0 \\ -\sin(B_0)\cos(L_0) & -\sin(B_0)\sin(L_0) & \cos(B_0) \\ \cos(B_0)\cos(L_0) & \cos(B_0)\sin(L_0) & \sin(B_0) \end{bmatrix}$ expresses the matrix of coordinate transformation, $\mathbf{x}_0 = [x_0, y_0, z_0]^T$ is the origin of coordinates, and B_0 and L_0 are the latitude and longitude of \mathbf{x}_0 . The calculation method of $e_{k-1}, n_{k-1},$ and u_{k-1} can refer to equation (25). Therefore, inequations (22) to (24) can be derived as

$$(\mathbf{I}_3 \otimes \mathbf{R})\mathbf{T}\mathbf{x}_k \leq (\mathbf{I}_3 \otimes \mathbf{R})\mathbf{T}\mathbf{x}_{k-1} + \boldsymbol{\Theta} \tag{26}$$

where $\boldsymbol{\Gamma}_k = (\mathbf{I}_3 \otimes \mathbf{R})\mathbf{T}$ with $\mathbf{R} = [1, -1]^T$ and $\mathbf{G}_k = (\mathbf{I}_3 \otimes \mathbf{R})\mathbf{T}\mathbf{x}_{k-1} + \boldsymbol{\Theta}$ with $\boldsymbol{\Theta} = [\alpha_2, -\alpha_1, \beta_2, -\beta_1, \gamma_2, -\gamma_1]^T$. It is worth mentioning that there are two sub-constraints in the E, N, and U directions, respectively, and the two sub-constraints in each direction mentioned above cannot be unsatisfied simultaneously. In addition, since the algorithm is highly dependent on the estimated coordinates of previous epochs, the algorithm startup time and reference value need to be reasonably set in advance, especially in real-time and kinematic situations. It is also worth noting that in real applications, if there are other parameters to be estimated, such as ambiguities, it only needs to augment zero matrices in $\boldsymbol{\Gamma}_k$. Also, one can use other inequality constraints according to the situation. Hence, in theory, GNSS precise positioning

Table 1 RTK common processing strategies

Items	Strategies
Observations used	GPS: C1C/L1C/C2X/L2X BDS: C2I/L2I/C7I/L7I
Ephemeris used	Broadcast ephemeris
Cut-off elevation	15°
Tropospheric correction	Saastamoinen model
Ionospheric correction	Klobuchar model
Positioning mode	EKF
Ambiguity resolution	LAMBDA

and navigation with inequality constraints is an important supplement in resilient PNT.

Experimental results and discussion

To verify the resilient RTK positioning model with equality and inequality constraints, we first introduce four datasets and their processing strategies. Then, two experiments are conducted and discussed.

Data description and experiment setup

The GNSS data from four landslide real-time kinematic monitoring stations in Sichuan, China, were selected to assess the performance of the proposed method. The observation conditions of these four datasets are not good enough which will be shown below. All stations used the same type of receiver, of which the board is MXT906B. The board supports the original observation output and has a small size and low power consumption characteristics. The receiver adopts an integrated design with built-in GNSS full-band antennas and a low-cost board. The sample interval of the four datasets was 5 s, and the duration was 24 h.

The RTK mode is used to verify the effectiveness of the new approach. The receiver can receive dual-frequency data from GPS and BDS; thus, this study conducted GPS/BDS dual-frequency RTK experiments. Table 1 gives detailed common processing strategies of the traditional method without inequality constraints and the proposed method with inequality constraints. The experiments are performed by our self-developed software C-RTK (Canyon RTK) (Zhang et al. 2022c). Tropospheric and ionospheric delays are corrected by the empirical models. The baseline solutions are estimated using the EKF strategy, and the modified least squares ambiguity decorrelation adjustment (LAMBDA) (Teunissen 1995; Chang et al. 2005) is adopted here.

Figure 1 shows the baseline information of the four datasets, where the receiver diagram is shown in the top subplot. It can be seen that it is an integrated receiver with built-in

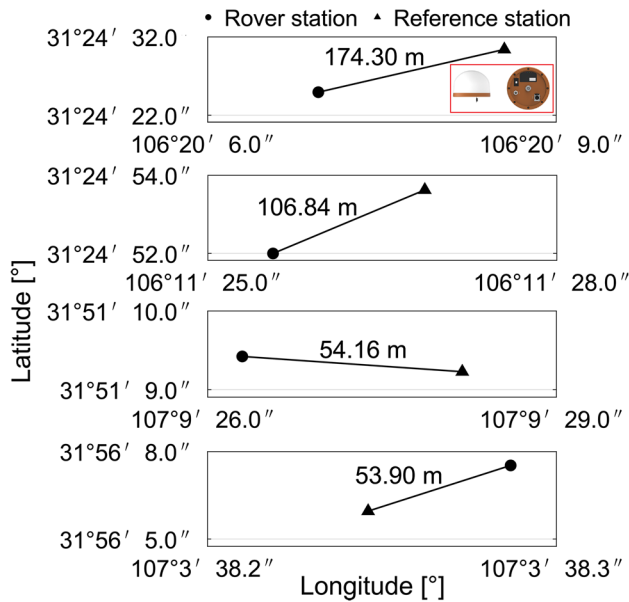


Fig. 1 Baseline information of the four datasets No. 1 to No. 4 (from top to bottom). The triangle and circle denote the rover and reference stations, respectively. The receiver diagram of the integrated receiver with built-in GNSS antennas is shown in the top subplot

GNSS antennas. Each rover station has its reference station, where the baseline lengths are all shorter than 200 m. The purpose of using a short baseline in landslide monitoring is to eliminate atmospheric delays since there are other positioning problems caused by multipath, NLOS reception, and other residual errors in such canyon environments. The coordinates of the four rover stations have been accurately determined in advance just validation, which have not been used by the software.

Figure 2 describes the changes in the number of satellites and position dilution of precision (PDOP) values of the four rover stations, where the situations of GPS, BDS, and total satellites are all included. Fewer GPS satellites were observed than BDS satellites in this study. The number of satellites fluctuates, but the total number exceeds 13, which meets the fundamental positioning requirements. As for the PDOP, since most of the PDOPs fluctuate between 1 and 3, the spatial distribution of satellites is acceptable. However, some sudden fluctuations still exist, especially in GPS, of which the value can reach 11.76. It indicates that some satellites greatly influence the PDOP value and even positioning accuracy.

Figure 3 shows the observed C/N_0 in terms of the sky plot for the four rover stations, in which only the observations with an elevation greater than 15° are shown. The top row of Fig. 3 is the sky plot of L1/B1 observations of four stations, while the bottom row is the sky plot of L2/B2 observations. It can be seen that the signals of the four stations are all reflected, refracted, diffracted, and even blocked to a

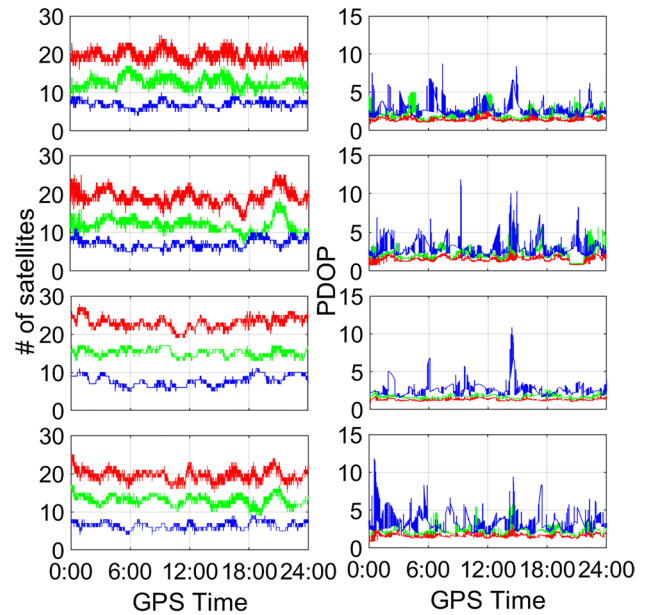


Fig. 2 Number of satellites (left) and PDOP values (right) of the four rover stations No. 1 to No. 4 (from top to bottom)

certain extent. Specifically, the C/N_0 values on the east side of stations No. 1 and No. 3 and the west side of No. 2 and No. 4 stations have apparent abnormal phenomena, such as signal attenuation (e.g., L1/B1) and interruption (e.g., L2/B2). Taking a closer look at Fig. 3, the C/N_0 values of L1/B1 in the attenuation direction are frequently smaller than 30 dB-Hz, especially when the elevations are lower than 30° . Moreover, even though the elevation is 60° , some C/N_0 values are still attenuated below 25 dB-Hz. It demonstrates that the signal reflection, refraction, and diffraction caused by dense trees in the natural environment are pronounced. In addition, the observations near the boundary of the obstacles are intermittent and even interrupted, indicating that the signals are blocked. Therefore, in the case of short baselines, there may still be many situations that can cause serious unmodeled errors in positioning results, and functional models may not obtain accurate and reliable positioning results without constraints.

Analysis of ambiguity resolution

First, the performance of ambiguity resolution is studied. For easy comparison, the ambiguity is initialized separately for each epoch. Hence, it facilitates the evaluation of ambiguity resolution at this time. Considering the actual landslide deformation speed, the annual landslide deformation in E, N, and U directions is usually less than 1 cm (Zhang et al. 2022a). Therefore, without loss of generality, the constraint parameters $\alpha_1, \alpha_2, \beta_1, \beta_2, \gamma_1$, and γ_2 are set to $-4, 4, -4, 4, -10$, and 10 , respectively, in a unit of centimeters. The threshold set

Fig. 3 Observed C/N_0 in terms of the sky plot for the rover stations No. 1 to No. 4 (from left to right). The top and bottom panels denote the results of L1/B1 and L2/B2, respectively

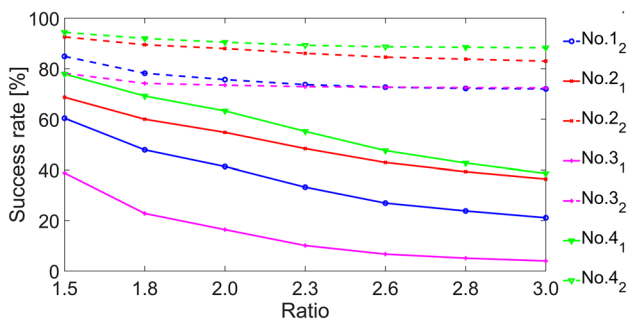
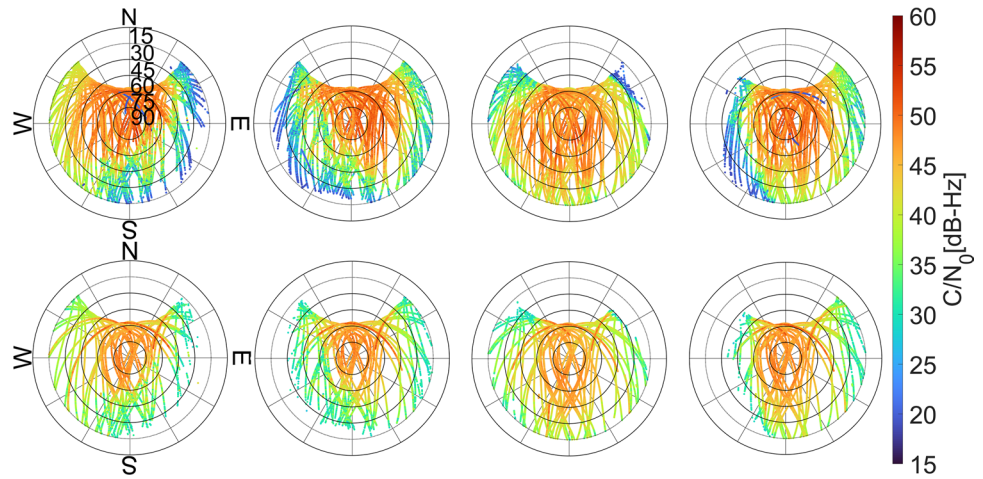


Fig. 4 Success rates of ambiguity resolution for the four rover stations under different ratios. The solid and dashed lines denote the results of the traditional method without inequality constraints and the proposed method with inequality constraints, respectively. The subscripts 1 and 2 in the legend denote the traditional and proposed methods, respectively

is relatively weak, and stronger constraints can be given for practical applications. Strong constraints are not used because we want to prove the effectiveness of inequality constraints. We give a practical strategy based on extensive research to determine the appropriate algorithm startup time and accurate reference value. The constraint algorithm will not be activated until the number of epochs is greater than 120 and there are at least 20 solutions with a ratio of squared norms between the second-best and best ambiguity candidates greater than 4.0 for insurance. Since the information from the previous epoch is not always reliable, the reference value is set as the average of the nearest conserved 20 solutions.

Table 2 Float ambiguities without and with inequality constraints (IC) and true integer ambiguities in a typical epoch (unit: cycle)

Ambiguity index	I	II	III	IV	V	VI	VII	VIII	IX	X
Without IC	12.91	-35.70	32.78	54.16	58.88	-75.44	-12.68	0.41	-34.85	2.26
With IC	11.11	-45.83	30.30	44.71	57.00	-81.93	-18.64	3.14	-38.63	3.93
Reference	11	-46	30	44	57	-82	-19	3	-39	4

Figure 4 shows the success rates of ambiguity resolution for the four datasets at ratios set to 1.5, 1.8, 2.0, 2.3, 2.5, 2.8, and 3.0, where the solid and dashed lines denote the results of the traditional method without inequality constraints and the proposed method with inequality constraints, respectively. It can be seen that the proposed method can significantly improve the success rates regardless of the ratio setting. Specifically, the success rates of the four stations solved by the proposed method are all above 72.0% and increased by 42.2% on average. Dataset No. 3 has the most significant improvement in success rates, with an average increase of 58.9%. Moreover, when the ratio is set to 3.0, the success rate is originally only 4.0%, and later is improved by 68.4%. Therefore, it demonstrates the effectiveness of the resilient positioning with inequality constraints since the float ambiguities are improved to a great extent by restricting the coordinate components.

Table 2 lists the changes of part of float ambiguities before and after using the inequality constraints in a representative epoch in dataset No. 4, where the third row denotes the true integer ambiguities. After applying the validation of ambiguity resolution, the ratio increases from 1.51 to 2.69. Mean absolute deviation (MAD) and root mean square error (RMSE) are the indicators chosen to evaluate the performance of the positioning models. The expressions of the two accuracy indicators are defined as follows:

$$MAD = \frac{\sum_{\eta=1}^w |S_{\eta} - S_v|}{w} \tag{27}$$

Table 3 Statistics of the float solutions for the four rover stations without and with inequality constraints (IC) (unit: m)

Indicator	Direction	No. 1		No. 2		No. 3		No. 4	
		Without IC	With IC						
MAD	E	0.609	0.030	0.715	0.027	0.839	0.019	0.463	0.027
	N	0.604	0.025	0.504	0.017	0.917	0.023	0.413	0.024
	U	1.550	0.081	2.272	0.076	2.581	0.075	1.459	0.096
RMSE	E	1.041	0.036	1.397	0.033	1.207	0.023	0.997	0.033
	N	1.000	0.029	0.998	0.022	1.325	0.028	0.931	0.028
	U	2.608	0.091	4.447	0.099	3.721	0.081	3.246	0.108

$$RMSE = \sqrt{\frac{\sum_{\eta=1}^w (S_{\eta} - S_v)^2}{w}} \tag{28}$$

where S_v expresses the reference value, S_{η} the value of the η th data, and w the total amount of data. It can be seen that the float ambiguities of the proposed method are much closer to the reference integer values. Specifically, the mean MADs of float ambiguities without and with inequality constraints are 4.84 and 0.23 cycles, respectively. Therefore, the float ambiguities of the proposed method are much more reliable, which is beneficial to ambiguity resolution and thus can obtain higher positioning accuracy.

The corresponding statistics of the four rover stations are listed in Table 3, calculated from the start of the inequality constraints for equality. The threshold of the ratio test is 2.0. It can be seen that the accuracy of the traditional method without inequality constraints in the E, N, and U directions is only at the decimeter level or even meter level. In contrast, the proposed method with inequality constraints makes the positioning accuracy reach the centimeter level. The reason may be that the inequality constraints make calculating float ambiguities more reliable, thereby improving the success rates of ambiguity resolution and the accuracy of estimated coordinate parameters. It shows that introducing inequality constraints is essential because they can better estimate float ambiguities and are largely resistant to unmodeled errors.

Analysis of positioning performance

Then, the RTK positioning based on the fix-and-hold mode is adopted to analyze positioning performance comprehensively. According to the previous section, a more reliable float solution helps to improve the success rate of ambiguity resolution. Therefore, considering that the adopted positioning mode is highly dependent on the previous solutions, the last 100 solutions with a ratio greater than 4.0 are kept, and their average is taken as the reference value in this experiment. One can immediately start up the inequality constraints if there is enough accurate prior information, and vice versa. The other settings are the same as mentioned

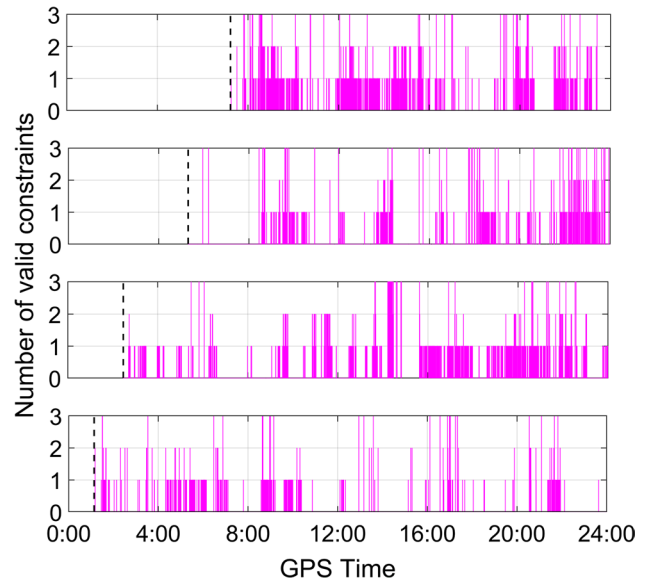


Fig. 5 Number of valid constraints of four datasets No. 1 to No. 4 (from top to bottom). The black dashed line denotes the start time of the proposed method

above. The threshold of the ratio test is 2.0. Figure 5 shows the number of valid constraints in each epoch of four datasets No. 1 to No. 4. It can be seen that the number of valid constraints has four cases: zero, one, two, and three. Since the two valid sub-constraints in each direction are mutually exclusive, it is reasonable that the valid constraints are less than or equal to three. The startup time of the proposed method in four datasets ranges from one to seven hours, indicating that the selected datasets are representative. In addition, the number of one, two, and three valid constraints in each dataset differs. For instance, the numbers of one, two, and three valid constraints of dataset No. 1 are 1200, 233, and 59, respectively, while those of dataset No. 4 are 544, 54, and 34, respectively. It implies that each dataset has many valid constraints; thus, the constraints set to these datasets are reasonable and necessary.

Table 4 lists the constraint process of two typical epochs in dataset No. 1, where the changes of J are recorded in

Table 4 Constraint process of two typical epochs

Epoch index	Valid constraint	Original ratio	Final ratio	J (m)				
				$s = 0$	$s = 1$	$s = 2$	$s = 5$	$s = 9$
I	1	1.9	2.0	-0.071	-0.071	-	-	-
				-0.008	-0.008	-	-	-
				-0.039	-0.040	-	-	-
				-0.040	-0.039	-	-	-
				-0.210	-0.200	-	-	-
				0.010	0.000	-	-	-
II	3	1.0	3.4	0.388	-0.006	-0.008	-0.011	-0.014
				-0.468	-0.073	-0.071	-0.068	-0.065
				-1.415	-0.084	-0.082	-0.081	-0.080
				1.335	0.004	0.002	0.001	0.000
				1.563	-0.002	-0.002	-0.003	-0.003
				-1.763	-0.197	-0.197	-0.196	-0.196

detail. Data in bold in Table 4 are the elements in J that do not satisfy the inequality constraints. Some conclusions can be drawn from the table: first, if the difference between the estimated parameters and the reference values is relatively small, such as epoch I, all the constraints can be satisfied within a few iterations. In this case, the proposed method only serves to fine-tune the float solutions, and in response, the ratio of this epoch is only increased by 0.1. Second, when the number of valid constraints is three, the corresponding point will likely have large deviations, like epoch II. After nine iterations, the estimated coordinate of epoch II finally satisfies the inequality constraints, and the ratio is also raised to 3.4. In addition, it can be seen from epoch II that the deviation of coordinates to be estimated is significantly reduced in the first few iterations, and the subsequent iterations are fine-tuning the coordinates until they fully meet the inequality constraints.

Figures 6, 7, 8, and 9 show the RTK positioning results of the traditional method without inequality constraints and the proposed method with inequality constraints of rover stations No. 1 to No. 4, respectively. Similarly, the dashed line in each figure marks the start time of the proposed method considering the inequality constraints. Bias in the figures refers to the difference between the positioning result and the reference value in an epoch, and it is signed. It can be seen that: first, as for rover station No. 1, there are many abnormal positioning results that the unmodeled errors may cause. At approximately 21:00, there is a period when the positioning results have significant deviations caused by the failure of ambiguity resolution. The proposed method starts at approximately 7:00 and suppresses most outliers. Second, similar to rover station No. 1, rover station No. 2 has many abnormal positioning results with deviations exceeding 1 m in the E , N , and U directions. The constraint algorithm is activated near 6:00, and there are no abnormal positioning results with deviations more

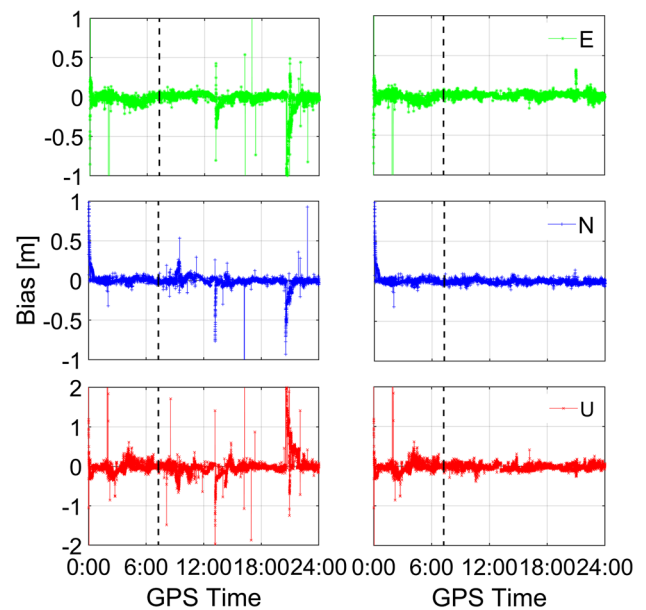


Fig. 6 RTK positioning results of the traditional method without inequality constraints (left) and proposed method with inequality constraints (right) in E , N , and U directions (from top to bottom) of the rover station No. 1. The black dashed lines denote the start time of the inequality constraints

significant than 1 m. Third, it is more challenging to deal with the problem of large positioning deviations over time, such as the original positioning results of rover station No. 3 from 15:00 to 22:00 when the deviations continuously reach 1 m. However, the positioning results are significantly improved using the inequality constraints, especially at 15:00. In this case, the reliability of the reference value and the validity of constraint parameters are proved. Then, the proposed method is activated in about one hour for rover station No. 4, reducing the noticeable deviations between 10:00 to 12:00 and 22:00.

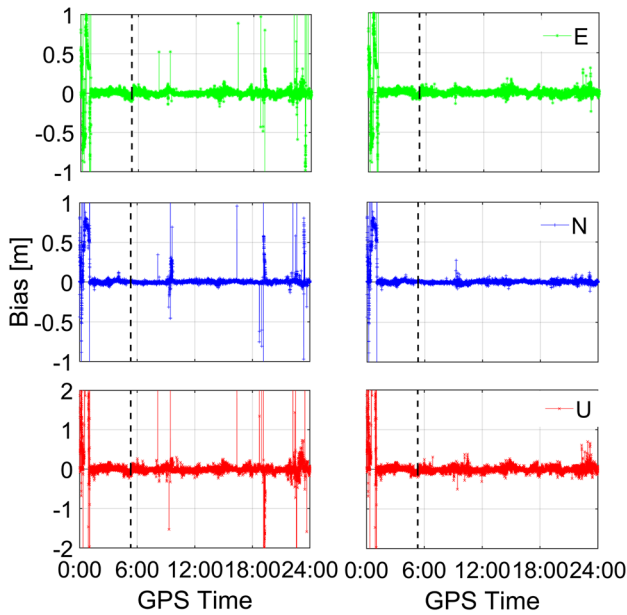


Fig. 7 RTK positioning results of the traditional method without inequality constraints (left) and proposed method with inequality constraints (right) in *E*, *N*, and *U* directions (from top to bottom) of the rover station No. 2. The black dashed lines denote the start time of the inequality constraints

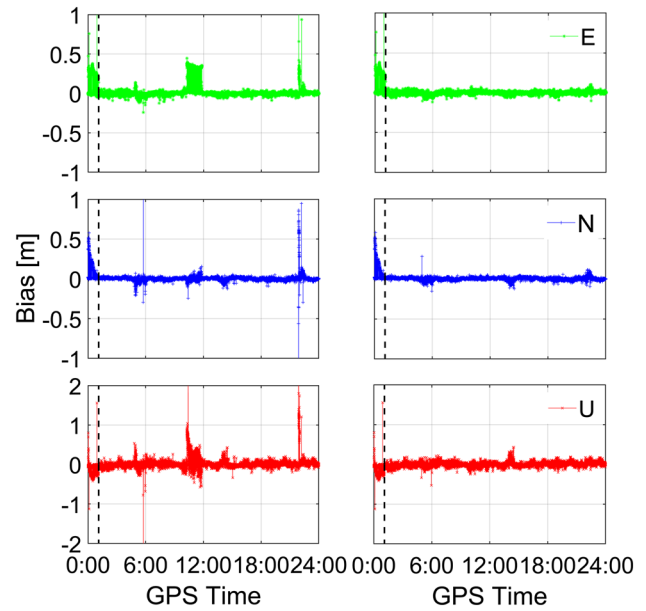


Fig. 9 RTK positioning results of the traditional method without inequality constraints (left) and proposed method with inequality constraints (right) in *E*, *N*, and *U* directions (from top to bottom) of the rover station No. 4. The black dashed lines denote the start time of the inequality constraints

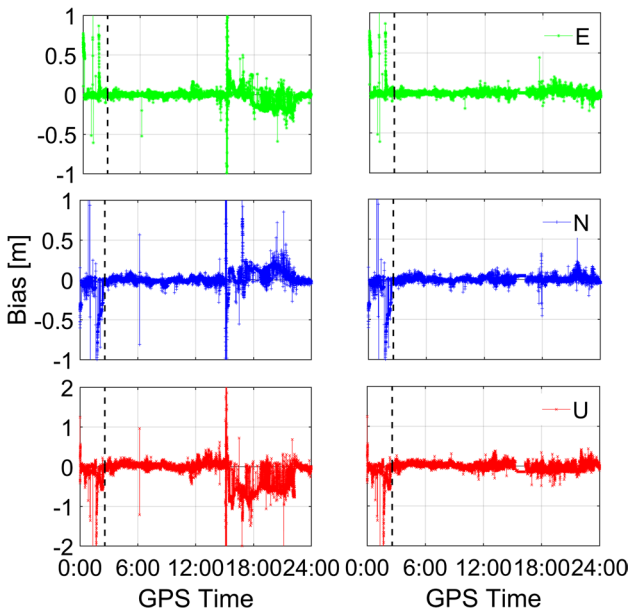


Fig. 8 RTK positioning results of the traditional method without inequality constraints (left) and proposed method with inequality constraints (right) in *E*, *N*, and *U* directions (from top to bottom) of the rover station No. 3. The black dashed lines denote the start time of the inequality constraints

As for the improved positioning results of the four rover stations, the proposed method still cannot wholly eliminate all abnormal positioning results. The main reason may be that

after obtaining the RTK float solution using the EKF method, the next step is to fix the ambiguities. During this process, there is still the possibility that ambiguities cannot be fixed, which in turn affects the acquisition of accurate coordinates. However, this problem can still be resolved if the inequality constraints are added to the fixed solutions though they are not shown here. In short, considering the inequality constraints, the proposed method can significantly preserve the accurate original positioning results and suppress the large positioning deviations according to the specific situation of each rover, thus being accurate and reliable.

To further quantitatively compare the performance of the two positioning models, the statistical results of the fixed solutions for the four rover stations are shown in Table 5. It can be seen that: first, the traditional positioning accuracy of the four rover stations is only up to the decimeter level due to a certain number of outliers and significant deviations over some time. After introducing the inequality constraints, the accuracy can meet the centimeter-level requirements. Of course, the accuracy is affected to some extent by the six constraint parameters. Second, the MAD of the four rover stations has an average decrease of 49.7%, 44.5%, and 49.7% in *E*, *N*, and *U* directions, respectively, and the corresponding RMSE has reduced by 78.1%, 73.5%, and 76.9% on average, respectively. To sum up, the proposed method can significantly improve the accuracy when the original positioning results have apparent large positioning errors.

Table 5 Statistics of the fixed solutions for the four rover stations without and with inequality constraints (IC) (unit: m)

Indicator	Direction	No. 1		No. 2		No. 3		No. 4	
		Without IC	With IC						
MAD	<i>E</i>	0.056	0.021	0.025	0.021	0.054	0.018	0.028	0.013
	<i>N</i>	0.037	0.018	0.018	0.011	0.059	0.023	0.015	0.011
	<i>U</i>	0.137	0.055	0.076	0.048	0.229	0.069	0.062	0.042
RMSE	<i>E</i>	0.159	0.028	0.096	0.029	0.160	0.026	0.077	0.018
	<i>N</i>	0.076	0.022	0.082	0.015	0.168	0.033	0.041	0.016
	<i>U</i>	0.372	0.067	0.354	0.066	0.488	0.086	0.145	0.055

Concluding remarks

We propose an easy-to-implement resilient real-time kinematic precise positioning method with inequality and equality constraints in challenging environments. Specifically, the basic methodology of the resilient RTK is proposed, and a practical form of inequality constraints in the real-time kinematic situation is given.

According to the four real datasets in challenging environments, the proposed methods can significantly improve success rates of ambiguity resolution and positioning accuracy. Specifically, since the inequality constraints make the float ambiguities more reliable, more than 72.0% of ambiguities can be fixed successfully, where approximately 42.2% improvement is obtained. For the fixed solutions, the proposed method can significantly preserve the accurate original positioning results and suppress the large positioning deviations according to the specific situation of each rover station, where the average improvement rates of MAD and RMSE for the four datasets are approximately 49.6% and 77.2%, respectively. In future, this method can also be applied to other positioning modes such as network RTK, precise point positioning (PPP) and even PPP-RTK, where different types of inequality constraints may need to be proposed.

Acknowledgements This work was supported by the National Natural Science Foundation of China (42004014) and the Natural Science Foundation of Jiangsu Province (BK20200530).

Author contributions ZZ derived the formulae, proposed the methods, developed the software, and wrote the paper. YL developed the software, worked out the technical details, and wrote the paper. XH and LH designed the experiments and modified the original manuscript. All authors approved of the manuscript.

Data availability The experimental data of this study are available from the corresponding author for academic purposes on reasonable request.

Declarations

Conflict of interest The authors declare no conflict of interest.

References

- Chang X, Yang X, Zhou T (2005) MLAMBDA: a modified LAMBDA method for integer least-squares estimation. *J Geod* 79(9):552–565
- Chang L, Niu X, Liu T, Tang J, Qian C (2019) GNSS/INS/LiDAR-SLAM integrated navigation system based on graph optimization. *Remote Sens* 11(9):1009
- Lau L, Cross P (2007) Development and testing of a new ray-tracing approach to GNSS carrier-phase multipath modelling. *J Geod* 81(11):713–732
- Leick A, Rapoport L, Tatarnikov D (2015) GPS satellite surveying. John Wiley & Sons, Hoboken
- Li B, Zhang Z, Shen Y, Yang L (2018) A procedure for the significance testing of unmodeled errors in GNSS observations. *J Geod* 92(10):1171–1186
- Lu G, Krakiwsky E, Lachapelle G (1993) Application of inequality constraint least squares to GPS navigation. *Manuscripta Geod* 18:124–130
- Luo X, Mayer M, Heck B, Awange J (2014) A realistic and easy-to-implement weighting model for GPS phase observations. *IEEE Trans Geosci Remote Sens* 52(10):6110–6118
- Ma L, Lu L, Zhu F, Liu W, Lou Y (2021) Baseline length constraint approaches for enhancing GNSS ambiguity resolution: comparative study. *GPS Solut* 25:40
- Marques H, Monico J, Aquino M (2011) RINEX_HO: second- and third-order ionospheric corrections for RINEX observation files. *GPS Solut* 15(3):305–314
- Meguro J, Murata T, Takiguchi J, Amano Y, Hashizume T (2009) GPS multipath mitigation for urban area using omnidirectional infrared camera. *IEEE Trans Intell Transp Syst* 10(1):22–30
- Ng H, Hsu L (2021) 3D mapping database-aided GNSS RTK and its assessments in urban canyons. *IEEE Trans Aerosp Electron Syst* 57(5):3150–3166
- Petovello M, Lachapelle G (2006) Comparison of vector-based software receiver implementations with application to ultra-tight GPS/INS integration. In: Proceedings of the 19th international technical meeting of the satellite division of the institute of navigation (ION GNSS 2006), pp 1790–1799
- Saurabh G (2006) Performance evaluation of low cost MEMS-based IMU integrated with GPS for land vehicle navigation application. *MASTER Diss Calg Alta* 12(2):37–45
- Schön S, Brunner F (2008) Atmospheric turbulence theory applied to GPS carrier-phase data. *J Geod* 82(1):47–57
- Sun R, Wang G, Cheng Q, Fu L, Chiang K, Hsu L, Ochieng W (2021) Improving GPS code phase positioning accuracy in urban environments using machine learning. *IEEE Internet Things J* 8(8):7065–7078
- Teunissen P (1995) The least-squares ambiguity decorrelation adjustment: a method for fast GPS integer ambiguity estimation. *J Geod* 70(1–2):65–82

- Teunissen P, Giorgi G, Buist P (2011) Testing of a new single-frequency GNSS carrier phase attitude determination method: land, ship and aircraft experiments. *GPS Solut* 15(1):15–28
- Wang L, Groves P, Ziebart M (2015) Smartphone shadow matching for better cross-street GNSS positioning in urban environments. *J Navig* 68(3):411–433
- Xie J, Lin D, Long S (2022) Total least squares adjustment in inequality constrained partial errors-in-variables models: optimality conditions and algorithms. *Surv Rev* 54(384):209–222
- Yang Y (2018) Resilient PNT concept frame. *Acta Geod Cartogr Sin* 47(7):893–898
- Zhang Z, Li B (2020) Unmodeled error mitigation for single-frequency multi-GNSS precise positioning based on multi-epoch partial parameterization. *Meas Sci Technol* 31(2):025008
- Zhang Z, Li B, Gao Y, Shen Y (2019) Real-time carrier phase multipath detection based on dual-frequency C/N0 data. *GPS Solut* 23:7
- Zhang Q, Bai Z, Huang G, Du Y, Wang D (2022a) Review of GNSS landslide monitoring and early warning. *Acta Geod Cartogr Sin* 51(10):1985–2000
- Zhang X, Zhou Y, Zhu F, Hu H (2022b) A new vehicle motion constraint model with parameter autonomous learning and analysis on inertial drift error suppression. *Acta Geod Cartogr Sin* 51(7):1249–1258
- Zhang Z, Li Y, He X, Chen W, Li B (2022c) A composite stochastic model considering the terrain topography for real-time GNSS monitoring in canyon environments. *J Geod* 96(10):79
- Zhong P, Ding X, Yuan L, Xu Y, Kwok K, Chen Y (2010) Sidereal filtering based on single differences for mitigating GPS multipath effects on short baselines. *J Geod* 84(2):145–158
- Zhou Z, Li B (2016) Optimal Doppler-aided smoothing strategy for GNSS navigation. *GPS Solut* 21:197–210
- Zhu J, Xie J (2011) A simple iterative algorithm for inequality constrained adjustment. *Acta Geod Cartogr Sin* 40(2):209–212
- Zhu J, Santerre R, Chang X (2005) A Bayesian method for linear, inequality-constrained adjustment and its application to GPS positioning. *J Geod* 78(9):528–534

Publisher's Note Springer Nature remains neutral with regard to jurisdictional claims in published maps and institutional affiliations.

Springer Nature or its licensor (e.g. a society or other partner) holds exclusive rights to this article under a publishing agreement with the author(s) or other rightsholder(s); author self-archiving of the accepted manuscript version of this article is solely governed by the terms of such publishing agreement and applicable law.



Zhetao Zhang obtained his Ph.D. with distinction from Tongji University. He is an Associate Professor at Hohai University, where his primary research focuses on precise positioning and navigation with GNSS and multi-sensor systems under complex conditions including challenging environments, low-cost devices, multi-source data, etc.



Yuan Li obtained a B.S. degree from the Suzhou University of Science and Technology in 2020. She is currently pursuing an M.S. degree in Geodesy at Hohai University, where her research directions are the GNSS precise positioning in canyon environment and GNSS meteorology.



Xiufeng He obtained a Ph.D. from Hong Kong Polytechnic University and is a Professor at Hohai University. Her research interests include deformation monitoring, multi-source data fusion, and integrated navigation.



Lita Hsu obtained a Ph.D. from National Cheng Kung University and is currently an Associate Professor at the Hong Kong Polytechnic University. His research interests include GNSS positioning in challenging environments and localization for pedestrians, autonomous driving vehicle, and unmanned aerial vehicle.